

Simulation of composite materials by a network FEM with error control

Martin Eigel, Daniel Peterseim

Angaben zur Veröffentlichung / Publication details:

Eigel, Martin, and Daniel Peterseim. 2015. "Simulation of composite materials by a network FEM with error control." Computational Methods in Applied Mathematics 15 (1): 21-37. <https://doi.org/10.1515/cmam-2014-0027>.

Nutzungsbedingungen / Terms of use:

licgercopyright

Dieses Dokument wird unter folgenden Bedingungen zur Verfügung gestellt: / This document is made available under the following conditions:

Deutsches Urheberrecht

Weitere Informationen finden Sie unter: / For more information see:

<https://www.uni-augsburg.de/de/organisation/bibliothek/publizieren-zitieren-archivieren/publizieren>



Research Article

Martin Eigel and Daniel Peterseim

Simulation of Composite Materials by a Network FEM with Error Control

Abstract: A novel finite element method (FEM) for the computational simulation in particle reinforced composite materials with many inclusions is presented. It is based on a specially designed mesh consisting of triangles and channel-like connections between inclusions which form a network structure. The total number of elements and, hence, the number of degrees of freedom are proportional to the number of inclusions. The error of the method is independent of the possibly tiny distances of neighboring inclusions. We present algorithmic details for the generation of the problem-adapted mesh and derive an efficient residual a posteriori error estimator which enables us to compute reliable upper and lower error bounds. Several numerical examples illustrate the performance of the method and the error estimator. In particular, it is demonstrated that the (common) assumption of a lattice structure of inclusions can easily lead to incorrect predictions about material properties.

Keywords: A Posteriori, Error Analysis, Finite Element Method, Composite Material, Multiscale, High Contrast, Generalized Delaunay, Network

MSC 2010: 65N15, 65N30, 74Q20

Martin Eigel: Weierstraß Institute, Mohrenstr. 39, 10117 Berlin, Germany, e-mail: eigel@wias-berlin.de

Daniel Peterseim: Institute for Numerical Simulation, Rheinische Friedrich-Wilhelms-Universität Bonn, Wegelerstr. 6, 53115 Bonn, Germany, e-mail: peterseim@ins.uni-bonn.de

1 Introduction

Particle reinforced composite materials are engineered materials which consist of different constituents with the aim to obtain physical properties better than what the used materials have on their own, i.e., a beneficial combination of the employed materials. The specific properties of the composite material strongly depend on macroscopic parameters such as the volume fraction and microscopic geometric features of the constituents. They thus represent a typical multiscale problem for analysis and computation.

For this paper, the effective conductivity of two-phase materials consisting of many randomly dispersed highly conducting filler particles (inclusions) and a poorly conducting binder material (matrix) shall be investigated. Typically, the matrix material exhibits favorable mechanical features while the inclusions determine the “functional” properties. For our purposes, the contrast of conductivity between inclusions and matrix is high, i.e., in our model we assume the inclusions to be ideal conductors.

Although there are many results about how to analyze problems of this kind if the microstructure of the material is structured or periodic (homogenization theory), see, e.g., [15, 16] and [3, 4, 11, 23], the mathematical treatment is much less clear for unstructured distributions of particles. In particular, phenomena specific to the lack of a regular structure play a crucial role since they can be responsible for drastic changes in material properties when the composition of the material is changed only slightly. One such well-known phenomenon is the percolation effect [14, 17] which can be observed for densely packed filler particles which occasionally form connected paths and thus strongly amplify the conducting property, see [5, 7].

Since the prediction of the behavior of a composite material on the one hand is crucial during the engineering process but on the other hand often is intractable analytically, numerical simulations can provide valuable insights with regard to effective material properties. Additionally, they can provide convenient means to test many different set-ups with the aim to obtain a specific material behavior.

For the Poisson-type model problem with discontinuous diffusion coefficient (introduced in the next section), a classical numerical method is the finite element method (FEM) which is based on a partition of the domain. In order to achieve accurate numerical results, the employed mesh would have to resolve the microscopic geometric structure of the problem. Since inclusions are irregularly distributed in the matrix and their volume fraction is large, they often are close to touching one another. The material responses depend crucially on these tiny distances. Thus, they have to be resolved accurately by the underlying mesh for the simulation to be reliable. The generation of a mesh appropriate for numerical simulation for such a domain is difficult and requires the use of many elements which consequently leads to a (possibly prohibitively) high complexity in the solution process, see Figure 1 for a simple setting which already requires a very large number of mesh elements. As can be observed, the diameter of the smallest FEM elements in Figure 1 scales at most like the minimal distance between inclusions.

Moreover, since the distribution of particles may be based on a random distribution, in order to determine the characteristic properties of a certain set-up, a large set of realizations of the geometry has to be evaluated for the calculation of expected properties. Thus, the complexity for the required mesh generation and the resulting (linear) algebraic system to be solved are crucial and limiting factors.

The method promoted in this article is capable to yield accurate and reliable results for the described problem with low computational complexity. This is achieved by a specific partition of the domain which is inspired by discrete network methods [5, 7, 8] (we refer to the recent textbook [6] for an overview on this methodology) and resolves the inclusions exactly while still remaining close to the classical FEM, both in implementation and the analytical results. For details regarding the a priori analysis, see [21]. Figure 1 also shows the adapted mesh which is of nearly optimal complexity, i.e., the number of elements is proportional to the number of inclusions. In particular, the complexity does not scale with the infinitesimal distance between inclusions. This is in contrast to what would have to be expected with standard FEM. There, a small distance between inclusions necessitates a strong refinement of the mesh so that elements sizes are of the order of the distance. This is required so that elements do not deteriorate and the domain is approximated sufficiently accurate. Despite the lower number of degrees of freedom, the discrete Network FEM (NFEM) model accounts for the complexity of the microstructure and provides a good overall macroscopic response, see Sections 2 and 3.

1.1 Model Problem

We consider the Poisson model problem on some perforated domain $\Omega \subset \mathbb{R}^2$ which results from some simply connected polygonal domain $\Omega^* \subset \mathbb{R}^2$ by removing a union of circular inclusions Ω_{inc} .

The set of closed, pairwise disjoint discs with positive radii is denoted by \mathcal{B}_{inc} , i.e., for any $B_1, B_2 \in \mathcal{B}_{\text{inc}}$ with $B_1 \neq B_2$,

$$B_1, B_2 \subset \Omega \quad \text{and} \quad \text{dist}(B_1, B_2) > 0.$$

The two phases of the material are represented by the set of the inclusions Ω_{inc} and the so-called matrix Ω ,

$$\Omega_{\text{inc}} := \bigcup_{B \in \mathcal{B}_{\text{inc}}} \text{int}(B) \quad \text{and} \quad \Omega := \Omega^* \setminus \overline{\Omega_{\text{inc}}}.$$

We assume the number of inclusions $N_{\text{inc}} := \#\mathcal{B}_{\text{inc}}$ to be very large such that Ω_{inc} occupies a significant amount of the volume of Ω^* . The problem then reads

$$-\text{div} \nabla u = f \quad \text{in } \Omega, \tag{1.1a}$$

$$u = u_D \quad \text{on } \Gamma_D, \tag{1.1b}$$

$$\partial_n u \cdot n = 0 \quad \text{on } \Gamma_N, \tag{1.1c}$$

$$u|_{\partial B} \equiv \text{const} \quad \text{and} \quad \int_{\partial B} \frac{\partial u}{\partial n_B} ds = 0 \quad \text{for all } B \in \mathcal{B}_{\text{inc}}, \tag{1.1d}$$

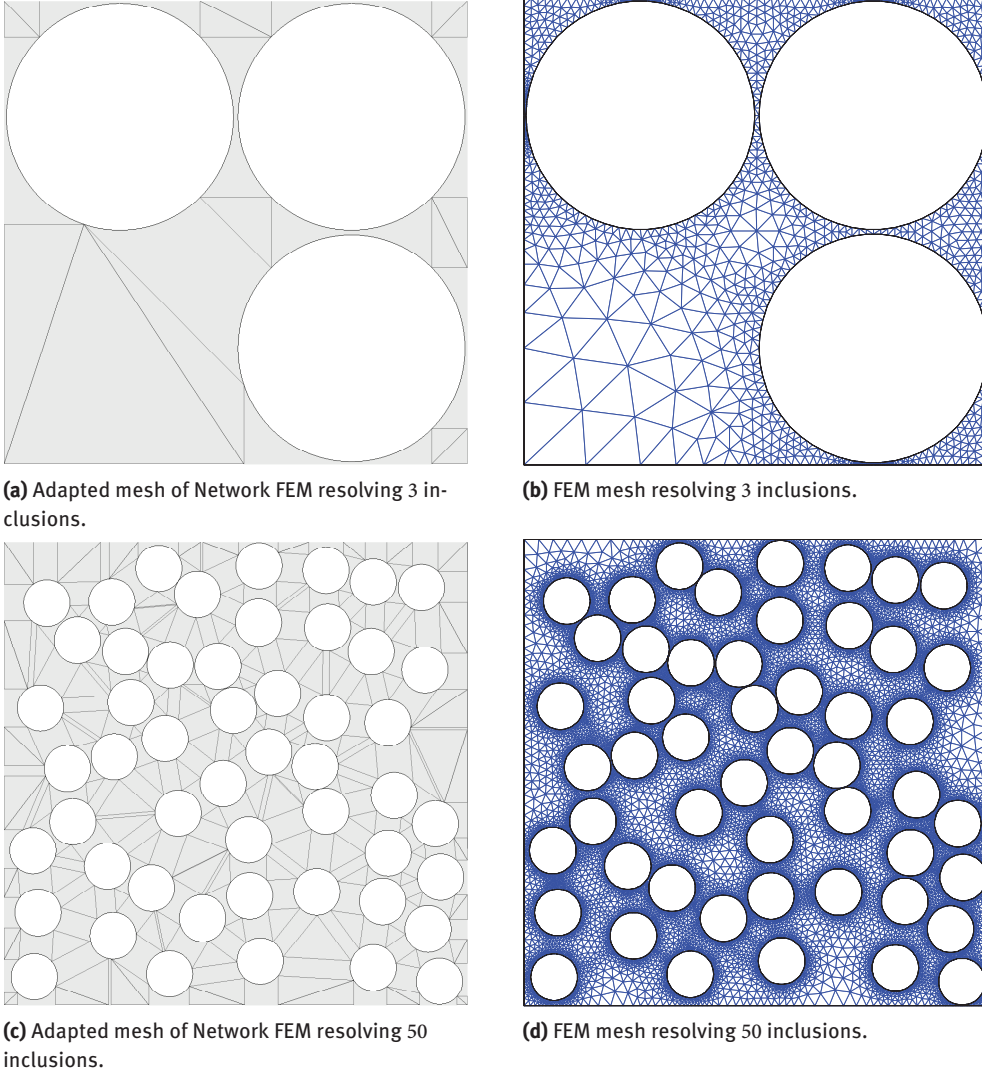


Figure 1. Illustration of the mesh complexity for FEM and Network FEM based on two simple settings with 3 and 50 inclusions.

with $f \in L^2(\Omega)$, also see [5]. The outer normal to some Lipschitz domain ω is denoted by n_ω . We just write n if $\omega = \Omega$. Sufficiently smooth Dirichlet boundary data u_D is imposed on the closed set $\Gamma_D \subset \partial\Omega^*$ with positive surface measure while homogeneous Neumann data is prescribed on $\Gamma_N := \partial\Omega^* \setminus \Gamma_D$. To reduce technical overhead, we will assume later that u_D is included in our discrete space, i.e., u_D is piecewise affine with respect to some subdivision of Γ_D . Otherwise, errors due to the approximation of the boundary values have to be considered.

Define the vector space

$$V := \{v \in H^1(\Omega) \mid v|_{\Gamma_D} = 0 \text{ and } \forall B \in \mathcal{B}_{\text{inc}} \exists k_B \in \mathbb{R} : v|_{\partial B} = k_B\}.$$

Note that any $v \in V$ has a unique extension $v^* \in H^1(\Omega^*)$ with $v^*|_\Omega = v$ and $\nabla v^*|_{\Omega^* \setminus \Omega} = 0$ because the trace of u on the boundary of an inclusion is constant. The variational formulation of (1.1) reads: Find $u \in u_D + V$ such that, for all $v \in V$,

$$a(u, v) := \int_{\Omega} \nabla u \cdot \nabla v \, dx = \int_{\Omega} f v \, dx =: F(v). \quad (1.2)$$

Using the Friedrichs' inequality, the coercivity of the continuous bilinear form a can readily be seen by

$$a(v, v) = \int_{\Omega} |\nabla v|^2 dx = \int_{\Omega^*} |\nabla v^*|^2 dx \geq \|v^*\|_{H^1(\Omega^*)}^2 \geq \|v\|_{H^1(\Omega)}^2$$

for $v \in V$. This coercivity along with the symmetry and boundedness of a , and the boundedness of F imply the unique solvability of equation (1.2).

Note that the unique weak solution u of formulation (1.1) is also the unique minimizer of the quadratic energy functional

$$\mathcal{E}(v) := \frac{1}{2} \int_{\Omega} |\nabla v(x)|^2 dx - \int_{\Omega} f(x)v(x) dx$$

amongst all $v \in u_D + V$.

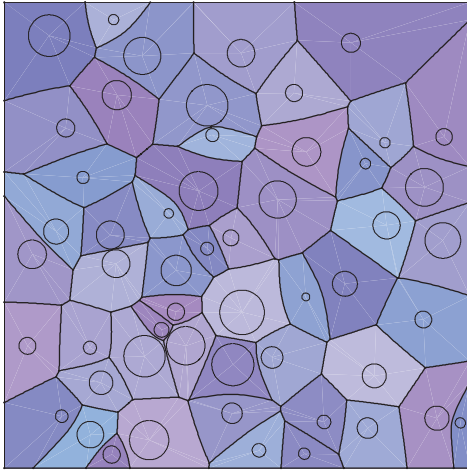
1.2 Outline and Contributions

Section 2 presents the novel Network FEM (NFEM). Complementary to the theoretical work in [21], we pursue a practical approach which includes algorithmic details regarding the actual implementation of the NFEM. These have not been described elsewhere and it is our hope that the presentation fosters the popularity of this promising numerical approach. We describe the underlying subdivision which exactly represents the geometry of the domain. The globally continuous approximation space is build as the union of local transformations of affine spaces on parametrized quadrilaterals (the “channels” between inclusions) and triangles. The crucial point is that *the dimension of the resulting space is the same as the number of inclusions due to the construction of the adapted mesh*. Thus, the complexity of the discretization is proportional to the complexity of the geometry representation (centers and radii of inclusions) and, hence, (quasi-)minimal. Interpolation error estimates and a priori error bounds are recalled. Section 3 is concerned with the derivation of some residual a posteriori error estimator which provides a computable error bound of the error of the discrete solution, see, e.g., [9] for similar results in the context of classical FEM and for further references. We prove reliability and efficiency of the error estimator which, while being based on arguments from classical FEM, requires some new non-trivial and non-standard estimates due to the specific features of the mesh. This new result opens the door to research in adaptive algorithms for the NFEM which can lead to very efficient and accurate numerical simulations in composite materials. Numerical validation of the Network FEM and the a posteriori error estimator is given in Section 4. The percolation phenomenon is shown experimentally. It can be observed when the inclusions reach a very high density such that they are in contact with neighboring inclusions. A remarkable observation is that the common modelling assumption of a structured distribution leads to fundamentally different results than random distributions of inclusions even when the volume fraction is identical. We finish in Section 5 with some conclusions and an outlook.

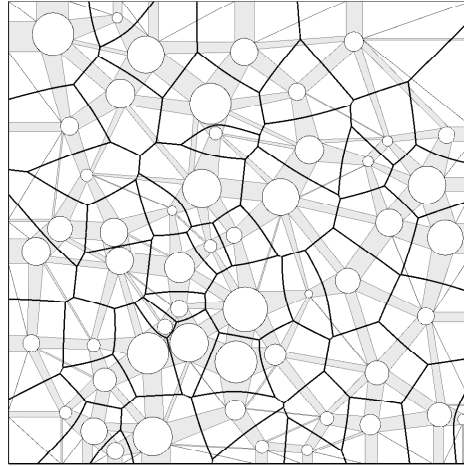
1.3 Notation

We use the common notation for Sobolev spaces of functions defined on a domain $\Omega \subset \mathbb{R}^2$. The space $H^k(\Omega)$ consists of all functions in $L^2(\Omega)$ which exhibit weak derivatives up to order k in $L^2(\Omega)$.

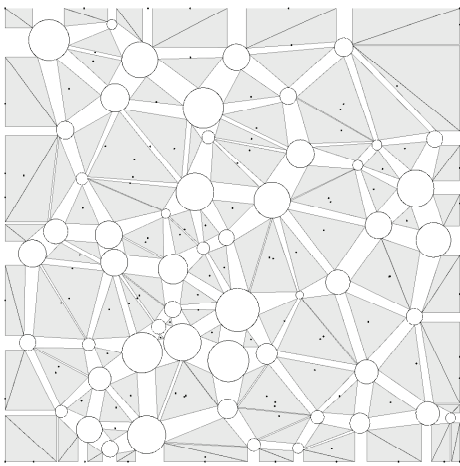
In estimates, the notation $A \lesssim B$ abbreviates $A \leq CB$ with some multiplicative constant $C > 0$ which only depends on the domain Ω and its shape but not on the mesh size h of finite element domains. Furthermore, $A \approx B$ abbreviates $A \lesssim B \lesssim A$.



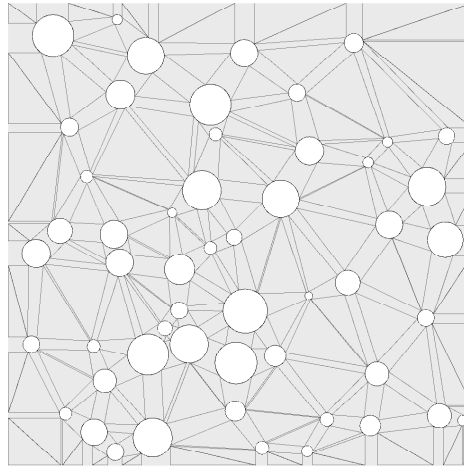
(a) Generalized Voronoi cells for set \mathcal{B} of discs.



(b) Isoparametric quadrilaterals \mathcal{Q} (shaded in gray) connecting any two discs of \mathcal{B} which are associated to some Voronoi edge in \mathcal{E}_* (black curves).



(c) Triangles \mathcal{T} (shaded in gray) associated to Voronoi vertices (black dots) occupy the remaining space between quadrilaterals of \mathcal{Q} .



(d) Final grid $\mathcal{G} = \mathcal{Q} \cup \mathcal{T}$ (shaded in gray) consisting of isoparametric quadrilateral and triangular elements.

Figure 2. Illustration of the grid construction in Section 2.1.

2 Network FEM

In this section, we recall the problem-adapted mesh and the construction of the conforming first-order discrete approximation space [21]. The mesh has to take into account the geometrical features of the domain, i.e., many circular inclusions, which is achieved by a combination of curvilinear quadrilaterals and triangular elements.

2.1 Grid Construction

The underlying geometry of the problem is determined by the set of (finitely many) closed discs \mathcal{B} . Each $B \in \mathcal{B}$ is defined by its center $c_B = \text{mid}(B)$ and the radius $r_B := \text{diam}(B)/2 \geq 0$. Note that also discs with radius zero are admissible. The elements of \mathcal{B} are denoted as *generalized vertices*. They are partitioned into the set of

inclusions \mathcal{B}_{inc} and discs with vanishing radius \mathcal{B}_{mat} :

$$\mathcal{B} = \mathcal{B}_{\text{inc}} \cup \mathcal{B}_{\text{mat}} \quad \text{and} \quad \mathcal{B}_{\text{inc}} \cap \mathcal{B}_{\text{mat}} = \emptyset.$$

The set \mathcal{B}_{mat} contains points on the boundary of Ω necessary to represent the domain adequately, e.g., the corner points of the domain and all points where the boundary condition switches from Neumann to Dirichlet. In order to control the approximation quality locally, it would be possible to add additional interior points to the set \mathcal{B}_{mat} . This for instance could be done by an adaptive algorithm based on the residual error estimator described in Section 3. However, the presented theory does not cover this case although a generalization seems straightforward.

In the following we provide an algorithmic description for the generation of the generalized mesh of the Network FEM.

Voronoi diagram of the inclusions. Pivotal to the construction of an appropriate mesh for the complex geometry of the matrix $\Omega = \Omega_{\text{mat}}$ is the (additively weighted) Voronoi diagram with regard to the set of discs \mathcal{B} . We refer to [2, 12] and references therein. We mark sets of the Voronoi construction by a subscript \circ . In case of equi-sized discs, the Voronoi cells $C \in \mathcal{C}_\circ$ are defined by straight line segments which become curved when the disc radii differ, see Figure 2. Each Voronoi cell $C \in \mathcal{C}_\circ$ is defined by a set of Voronoi edges $E \in \mathcal{E}_\circ$ and each edge is defined by two Voronoi vertices in the set of Voronoi vertices $\mathcal{N}_\circ(\Omega)$. For notational convenience, we define the following maps which relate these entities.

$$\begin{aligned} \text{neighbors } B_1, B_2 \in \mathcal{B} : \quad & \mathcal{E}_\circ(B_1, B_2) \quad \text{unique Voronoi edge associated with } B_1, B_2, \text{ i.e.,} \\ & \mathcal{E}_\circ(B_1, B_2) := \{x \in \mathbb{R}^2 \mid \text{dist}(x, B_1) = \text{dist}(x, B_2) = \min_{B \in \mathcal{B}} \text{dist}(x, B)\}, \\ B \in \mathcal{B} : \quad & \mathcal{E}_\circ(B) \quad \text{set of Voronoi edges associated to disc } B, \text{ i.e.,} \\ & \mathcal{E}_\circ(B) := \{\mathcal{E}_\circ(B, B_1) \mid B_1 \in \mathcal{B} \text{ and } \mathcal{E}_\circ(B_1, B) \in \mathcal{E}_\circ\}, \\ E \in \mathcal{E}_\circ : \quad & \mathcal{N}_\circ(E) \quad \text{set of two vertices of edge } E, \\ E \in \mathcal{E}_\circ : \quad & \mathcal{B}(E) \quad \text{set of two neighboring discs, i.e., with } E = \mathcal{E}_\circ(B_1, B_2), \\ & x \in E \quad \text{dist}(x, B_1) = \text{dist}(x, B_2) = \min_{B \in \mathcal{B}} \text{dist}(x, B), \\ p \in \mathcal{N}_\circ : \quad & \mathcal{B}(p) \quad \text{set of neighboring discs, i.e.,} \\ & \mathcal{B}(p) = \{B \in \mathcal{B} \mid \text{dist}(p, B) = \min_{\tilde{B} \in \mathcal{B}} \text{dist}(p, \tilde{B})\}. \end{aligned}$$

Our construction process for the mesh (Algorithm 1) generates two types of elements. First, an isoparametric quadrilateral is obtained for each Voronoi edge $E \in \mathcal{E}_\circ$ which results in the set of quadrilaterals \mathcal{Q} . Second, the remaining polygonal areas $\Omega \setminus \bigcup \mathcal{Q}$ are decomposed into the set of triangles \mathcal{T} . The union then fulfils $\bigcup \mathcal{T} \cup \bigcup \mathcal{Q} = \Omega$ and we set $\mathcal{G} := \mathcal{Q} \cup \mathcal{T}$ the subdivision of Ω . The set of edges is denoted by \mathcal{E} , the restriction to interior edges is $\mathcal{E}_{\text{int}} := \{E \in \mathcal{E} \mid E \cap \Omega \neq \emptyset\}$ and the restriction to boundary edges on Γ is defined by $\mathcal{E}(\Gamma)$.

The notation and further details are provided in the following subsections. A similar construction in the context of the discrete network approximation method can be found in [5].

Local construction of quadrilaterals. For some Voronoi edge $E \in \mathcal{E}_\circ$ with Voronoi vertices $\{p_1, p_2\} = \mathcal{N}_\circ(E)$, the corresponding discs with centers $c_1, c_2 > 0$ are $\{B_1, B_2\} = \mathcal{B}(E)$. We connect center c_1 with p_1 and p_2 and denote the intersections with disc B_1 by a_1 and b_1 , respectively. The same is done with c_2 which results in a_2, b_2 . The channel-like element $Q_E \in \mathcal{Q}$ of edge E is then defined by the line segments $\overline{a_1 a_2} = \text{conv}\{a_1, a_2\}$, $\overline{b_1 b_2} = \text{conv}\{b_1, b_2\}$ and the sections on the discs B_1, B_2 which lie in between a_1, b_1 and a_2, b_2 , respectively.

This procedure has to be carried out for all edges $E \in \mathcal{E}_\circ$ and provides the set of curvilinear quadrilaterals \mathcal{Q} . Note that if either one or both of the discs deteriorate to a point, we obtain either a curvilinear triangle or a line segment. The latter case is discarded.

Remark 2.1. Note that the Voronoi dual edge might not be connected (see Figure 3). The same applies to the corresponding isoparametric quadrilaterals as can be seen in the same figure. We denote the number of connected components of $Q \in \mathcal{Q}$ by $K(Q)$. The parametrization from Definition 2.2 applies to every connected component of Q .

Algorithm 1. Geometry adapted mesh construction.

Require: domain Ω^* , set of discs \mathcal{B}

Return: mesh $\mathcal{G} = \mathcal{Q} \cup \mathcal{T}$ of $\Omega = \Omega^* \setminus \mathcal{B}$ into isoparametric quadrilaterals \mathcal{Q} and triangles \mathcal{T}

$(\mathcal{C}_o, \mathcal{E}_o, \mathcal{N}_o) \leftarrow$ compute Voronoi diagram for (Ω, \mathcal{B})

$\mathcal{Q} \leftarrow \emptyset, \mathcal{T} \leftarrow \emptyset$ {initialization}

for all $E \in \mathcal{E}_o$ **do**

$(B_1, B_2) \leftarrow \mathcal{B}(E)$ neighboring discs associated with E

$a, b \leftarrow$ vertices of E

$c_1, c_2 \leftarrow$ centers of B_1, B_2

$a_1, b_1 \leftarrow$ intersection of line segments $\overline{c_1 a}$ and $\overline{c_1 b}$ with ∂B_1

$a_2, b_2 \leftarrow$ intersection of line segments $\overline{c_2 a}$ and $\overline{c_2 b}$ with ∂B_2

$s_1 \leftarrow$ boundary segment of ∂B_1 between a_1 and b_1

$s_2 \leftarrow$ boundary segment of ∂B_2 between a_2 and b_2

$\mathcal{Q} \leftarrow \mathcal{Q} \cup$ isoparametric quadrilateral $(s_1, \overline{a_1 a_2}, s_2, \overline{b_2 a_2})$

end for

for all $P \in \mathcal{N}_o$ **do**

$\Lambda \leftarrow \mathcal{B}(P)$ discs associated with Voronoi vertex P

$c_1, \dots, c_n \leftarrow$ centers of discs $B \in \Lambda$

$A \leftarrow \emptyset$ {initialization}

for all $B \in \Lambda$ **do**

$c \leftarrow$ center of B

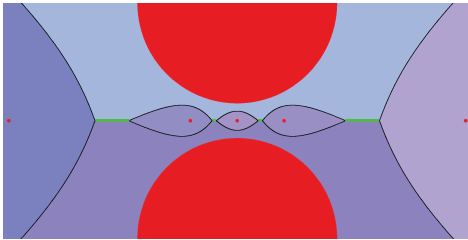
$A \leftarrow A \cup \{a\}$ intersection of line segment \overline{cP} with ∂B

end for

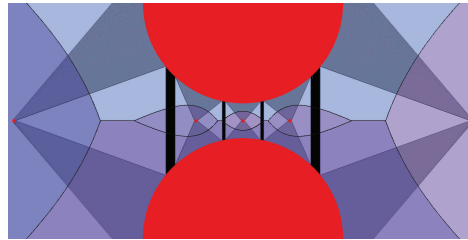
$\mathcal{T} \leftarrow \mathcal{T} \cup$ decomposition of $\text{conv}(A)$ into triangles

end for

$\mathcal{G} \leftarrow \mathcal{Q} \cup \mathcal{T}$



(a) Detail of a generalized Voronoi diagram with a multiply connected Voronoi edge.



(b) Detail of the corresponding finite element grid with multiply connected isoparametric quadrilateral (black shaded) T ($K(T) = 4$).

Figure 3. Generalized Voronoi and corresponding grid; Voronoi edges and corresponding isoparametric quadrilateral multiply connected.

Triangles. Algorithm 1 yields the set \mathcal{Q} and the entire surface of each disc is associated with a set of quadrilaterals from the set \mathcal{Q} , i.e., $\partial B = \bigcup_{Q \in \mathcal{Q}(B)} B \cap Q$ for any $B \in \mathcal{B}$. The remaining areas in Ω^* which are not occupied by either a disc or a quadrilateral are polygons. In fact, a polygon P_p with n edges is associated with each Voronoi vertex $p \in \mathcal{N}_o$ where $n = \#\mathcal{B}(p)$ and $P_p := \text{conv}\{a_1, \dots, a_n\}$ with a_1, \dots, a_n the intersection points of the connections of the disc centers of each $\mathcal{B}(p)$ with p . We decompose each such polygon into a set of triangles which results in the set \mathcal{T} . The adapted mesh is then given by $\mathcal{G} := \mathcal{Q} \cup \mathcal{T}$.

2.2 Mapping to Quadrilateral Elements

The result of the construction of the previous section is a set \mathcal{G} of elements which is a decomposition of the domain Ω . It consists of a set of isoparametric quadrilaterals \mathcal{Q} and a set of triangles \mathcal{T} . By \mathcal{E} we denote the set of edges of the elements of \mathcal{G} .

For the transformation from a reference rectangle $E^{\text{ref}} :=]\alpha, \beta[\times]0, 1[$ to curvilinear quadrilaterals (and triangles), we apply the following mapping.

Definition 2.2 (Mapping onto curvilinear quadrilaterals). Consider the circular inclusions $B_1, B_2 \in \mathcal{B}$, $B_1 \cap B_2 = \emptyset$, with radii r_1, r_2 and connecting quadrilateral $Q \in \mathcal{Q}$. The coordinate system can be rotated and shifted such that, without loss of generality, the centers of the discs are given by $c_1 = (0, 0)$ and $c_2 = (0, \delta)$ and $\delta > r_1 + r_2$. With angles $-\pi/2 \leq \alpha \leq \beta \leq \pi/2$ and $Q \in \mathcal{Q}$, define the map $J_Q :]\alpha, \beta[\times]0, 1[\rightarrow \text{int}(Q)$ by

$$J_Q(s, \lambda) := \left((1 - \lambda)r_1 + \lambda r_2 \frac{r_1 + H(s)}{r_2 + H(s)} \right) \begin{bmatrix} \sin(s) \\ \cos(s) \end{bmatrix} + \delta \lambda \left(1 - \frac{r_2}{r_2 + H(s)} \right) \begin{bmatrix} 0 \\ 1 \end{bmatrix},$$

where

$$H(s) := \frac{(\delta^2 - 2 \cos(s)\delta r_1) + r_1^2 - r_2^2}{(2r_2 - 2r_1) + 2\delta \cos(s)}.$$

See Figure 4 (left) for an illustration.

Local Mesh Size. For any triangle $T \in \mathcal{T}$, $h_T := \text{diam}(T)$ denotes its size parameter. Analogously, for any edge $E \in \mathcal{E}$, i.e., $h_E = \text{diam}(E)$. For $Q \in \mathcal{Q}$, the definition of the mesh size h_Q is more involved since it is subject to the mapping J_Q of Definition 2.2. We set, for $x \in Q$ and $(s, \lambda) = J_Q^{-1}(x)$,

$$h(x) := \|J_Q(s, 1) - J_Q(s, 0)\|_{\mathbb{R}^2}.$$

Note that h varies within each quadrilateral. Then, the piecewise continuous global mesh size function h is defined by

$$h|_G := h_G \quad \text{for } G \in \mathcal{G}.$$

Moreover, we define the vertex and edge patches

$$\begin{aligned} \omega_B &:= B \cup \{G \in \mathcal{G} : G \cap B \neq \emptyset\} \quad \text{for } B \in \mathcal{B}, \\ \omega_E &:= B \cup \{G \in \mathcal{G} : G \cap E \neq \emptyset\} \quad \text{for } E \in \mathcal{E}. \end{aligned} \tag{2.1}$$

2.3 Finite Element Space

The discrete approximation space has the same dimension as the cardinality of the set of vertices $|\mathcal{B}|$ of the mesh as in standard first-order FEM as defined below. Dirichlet boundary nodes are fixed and thus do not contribute to the dimension of the linear system. Associated to every $B \in \mathcal{B}$ is some basis function $\lambda_B : \Omega^* \rightarrow [0, 1]$ determined by the following conditions:

- (a) $\lambda_B \equiv 1$ on B and $\lambda_B \equiv 0$ on $\mathcal{B} \setminus B$,
- (b) $\lambda_B|_T$ is affine for all $T \in \mathcal{T}$,
- (c) $\lambda_B|_Q \circ J_Q$ is affine with respect to the reference element Q_{ref} for all $Q \in \mathcal{Q}$,
- (d) λ_B is continuous.

These basis functions generalize nodal basis functions on classical triangular meshes. The support of λ_B is given by

$$\text{supp}(\lambda_B) = B \cup \omega_B$$

with the vertex patch ω_B defined in (2.1).

The transformation of affine base functions on the reference rectangle Q_{ref} onto curvilinear quadrilaterals $Q \in \mathcal{Q}$ is achieved by the mapping J_Q of Definition 2.2. Figure 4 illustrates this mapping from some

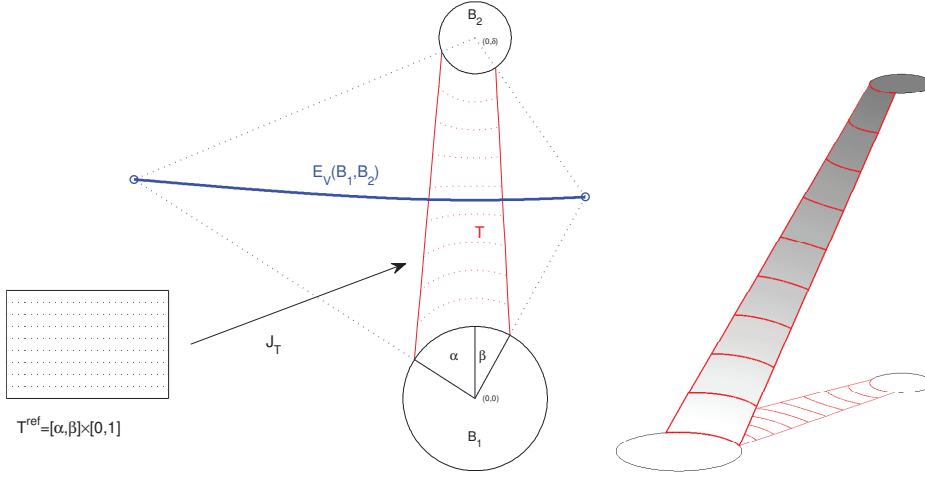


Figure 4. Map from reference rectangle to curvilinear quadrilateral (isolines) [left] and transformed affine base function restricted to some quadrilateral [right].

reference rectangle to the quadrilateral and a transformed base function associated to some node restricted to the quadrilateral.

The set of basis functions $\Lambda := \{\lambda_B : B \in \mathcal{B}\}$ forms a partition of unity in Ω . The finite element space

$$S := \text{span}(\Lambda) \cap V$$

is then spanned by the nodal basis functions λ_B of all $B \in \mathcal{B}$ which do not correspond to nodes on the Dirichlet boundary Γ_D .

The discrete problem reads: Find $u_{\text{NFEM}} \in u_D + V$ such that, for all $v \in V$,

$$a(u_{\text{NFEM}}, v) = F(v).$$

If u is sufficiently smooth, the error of the discrete solution $u_{\text{NFEM}} \in u_D + V$ satisfies [21]

$$\|\nabla(u - u_{\text{NFEM}})\|_{L^2(\Omega)} \lesssim \|h\nabla^2 u\|_{L^2(\Omega)}.$$

Moreover, the solution u satisfies [20]

$$\|h\nabla^2 u\|_{L^2(\Omega)} \lesssim \|f\|_{L^2(\Omega)} + \|u_D\|_{L^\infty(\partial\Omega)}.$$

We stress that the implicit constants in the previous two estimates do not depend on the tiny distances between neighboring inclusions.

3 A Posteriori Estimator

A posteriori error control allows to assess the quality of the discrete solution and provides upper and lower bounds for the global error. Although it is well established with standard FEM, see [1, 22], an extension to NFEM is not immediate. Instead, it requires the application of some non-trivial interpolation estimates as detailed in Section 3.1.

This section is concerned with the derivation of some residual a posteriori error estimator η based on a mesh \mathcal{G} . The aim of the estimator is to bound the error $e := u - u_{\text{NFEM}}$ in the energy norm. Two-sided bounds ensure that the estimator is sufficiently accurate.

Higher-order terms due to properties of the data enter the estimates in the form of oscillations. On some $G \in \mathcal{G}$, let $f_G := |G|^{-1} \int_G f \, dx$ be the average of $f \in L^2(\Omega)$ in G . The global \mathcal{G} -piecewise constant function $f_{\mathcal{G}}$ is defined by $f_{\mathcal{G}}|_G = f_G$ for $G \in \mathcal{G}$. Then, define oscillations on \mathcal{G} by

$$\text{osc}(f, \mathcal{G}) := \|h_{\mathcal{G}}(f - f_{\mathcal{G}})\|_{L^2(\Omega)}. \quad (3.1)$$

Define the computable interior residual r_G and the edge residual r_E by

$$r_G := f + \operatorname{div}_{\mathcal{G}} \nabla_{\mathcal{G}} u_{\text{NFEM}} \quad \text{in } G \in \mathcal{G},$$

$$r_E := \begin{cases} -\nabla u_{\text{NFEM}} \cdot n_E & \text{on } \mathcal{E}(\Gamma_N), \\ -\left[\nabla u_{\text{NFEM}} \cdot n_E \right]_E & \text{on all other } E \in \mathcal{E}, \end{cases}$$

and set $\tilde{r}_G := r_G + (f_G - f)$. By the subscript in $\operatorname{div}_{\mathcal{G}}$ and $\nabla_{\mathcal{G}}$ we denote the piecewise application of the differential operator.

The error estimator then reads

$$\eta := \left(\sum_{G \in \mathcal{G}} \|h_G r_G\|_{L^2(G)}^2 + \sum_{E \in \mathcal{E}} h_E \|r_E\|_{L^2(E)}^2 \right)^{1/2}.$$

We call an estimator *reliable* if $\|\nabla e\|_{L^2(\Omega)} \lesssim \eta$, and *efficient* if $\eta \lesssim \|\nabla e\|_{L^2(\Omega)}$.

The main result is the following theorem.

Theorem 3.1. *Given the discrete solution $u_{\text{NFEM}} \in u_D + V$, the a posteriori error estimator η is reliable and efficient, i.e., with oscillations (3.1), it holds*

$$\|\nabla(u - u_{\text{NFEM}})\|_{L^2(\Omega)} \lesssim \eta \quad \text{and} \quad \eta \lesssim \|\nabla(u - u_{\text{NFEM}})\|_{L^2(\Omega)} + \operatorname{osc}(f, \mathcal{G}).$$

Remark 3.2. The first estimate is independent of all mesh related parameters except the angles of the elements. The implicit constant in the second estimate depends on the geometry in the following sense. The constant is proportional to the maximal ratio of the distance of neighboring inclusions and their radii, i.e., the constant reflects the diameter of areas in the material with no inclusion relative to the radii of the inclusions. Since we are mainly interested in numerical experiments where the reliability of the estimator is crucial, we do not further investigate this issue.

The proof of the theorem is provided in Sections 3.2 and 3.3. The specific properties of the specially designed mesh and the respective discrete space impose complications in the derivation which are not encountered in standard FEM. This is reflected by the crucial fact that some norms are weighted by the mesh size h_T since it is non-constant on the elements $Q \in \mathcal{G}$.

In the following, we prove the reliability of the a posteriori estimator independent of the critical geometric parameters of Ω .

3.1 Interpolation

We will use the interpolation operator $I : V \rightarrow S$ defined for $v \in V$ by

$$Iv := \sum_{B \in \mathcal{B}_{\text{inc}}} v|_B \lambda_B + \sum_{b \in \mathcal{B}_{\text{mat}} \cap \Gamma_N} \left(|\omega_b| \int_{\omega_b} v dx \right) \lambda_b. \quad (3.2)$$

The operator I is well-defined for any function in $v \in V$, because $v|_B$ is not a point evaluation but the volume average of v on the inclusion $B \in \mathcal{B}_{\text{inc}}$. For vertices on the Neumann boundary, we perform standard Clément-type averaging. The resulting interpolation is locally stable in the following sense.

Lemma 3.3 (Stability of the interpolation). *For any $v \in V$ it holds*

$$\|\nabla Iv\|_{L^2(G)} \lesssim \|\nabla v\|_{L^2(\omega_G)} \quad \text{on any } G \in \mathcal{G},$$

where $\omega_G := \bigcup \{K \in \mathcal{G} \mid \bar{K} \cap \bar{G} \neq \emptyset\}$.

Proof for channel-like elements. Given any channel-like element $Q \in \mathcal{Q}$ (translated in space as in Definition 2.2), let $B_1, B_2 \in \mathcal{B}$ (with corresponding radii r_1, r_2) denote the inclusions connected by Q and let $v_1 := v|_{B_1}$,

$v_2 := v|_{B_2} \in \mathbb{R}$ denote the corresponding function values. Assume for the moment that the channel is parallel, i.e., the radii r_1 of B_1 and r_2 of B_2 are equal. Then it holds

$$\|\nabla I v\|_{L^2(Q)}^2 \approx \int_Q h(x)^{-2} |v_2 - v_1|^2 dx \leq \int_Q \underbrace{\left| \frac{v_2 - v_1}{h(x)} \begin{pmatrix} 0 \\ 1 \end{pmatrix} \right|^2}_{=: \sigma(x)} dx. \quad (3.3)$$

Since $r_1 = r_2$, the function $h(x) = h(x_1, x_2) = h(x_1)$ solely depends on the first component x_1 of the space variable $x \in Q$. Hence,

$$\sigma(x) := \frac{v_2 - v_1}{h(x)} \begin{pmatrix} 0 \\ 1 \end{pmatrix}$$

defines a divergence-free vector field in Q with $\sigma(x) \cdot n_Q = 0$ on $\partial Q \setminus (B_1 \cup B_2)$. We evaluate that

$$\int_Q \sigma^2 dx = \int_{\partial Q} v \sigma \cdot n_Q ds$$

and hence

$$\begin{aligned} \|\sigma\|_{L^2(Q)}^2 &= -\|\sigma\|_{L^2(Q)}^2 + 2 \int_{\partial Q} v \sigma \cdot n_Q ds \\ &\leq \sup \left\{ -\|\tilde{\sigma}\|_{L^2(Q)}^2 + 2 \int_{\partial Q} v \tilde{\sigma} \cdot n_Q ds \mid \tilde{\sigma} \in H(\operatorname{div}, Q) : \operatorname{div} \tilde{\sigma} = 0, (\tilde{\sigma}(x) \cdot n_Q)|_{\partial Q \setminus (B_1 \cup B_2)} = 0 \right\} \\ &= \inf \{ \|\nabla \tilde{v}\|_{L^2(Q)}^2 \mid \tilde{v} \in H^1(Q) : \tilde{v} = v \text{ on } \partial(B_1 \cup B_2) \} \leq \|\nabla v\|_{L^2(Q)}^2 \end{aligned}$$

by duality (see, e.g., [13]). The combination of this estimate and (3.3) yields the assertion for the parallel channel Q . The above arguments are easily generalized to the case of a non-parallel channel, i.e., $r_1 \neq r_2$, by choosing a suitable parallel channel $\tilde{Q} \subset Q$ and suitable adaptation of σ . If one of the inclusions is on the boundary, the result follows from Friedrichs' (Dirichlet boundary) or Poincaré's (Neumann boundary) inequality. In the latter case, the right-hand side may depend on v in some neighborhood ω_Q of Q . \square

Proof for triangles. Again, for elements $T \in \mathcal{T}$ where $T \cap \partial\Omega$ has positive length, the result follows directly from Friedrichs' or Poincaré's inequality.

Given any triangle $T \in \mathcal{T}$, choose $B_1, B_2 \in \mathcal{B}_{\text{inc}}$ amongst neighboring inclusions such that corresponding function values $v_1 := v|_{B_1}$, $v_2 := v|_{B_2}$ have maximal distance. Let $Q \in \Omega$ denote the element that connects the inclusions B_1 and B_2 . Then it holds

$$\|\nabla I v\|_{L^2(T)}^2 \lesssim |v_2 - v_1|^2 \lesssim \int_Q h(x)^{-2} |v_2 - v_1|^2 dx \approx \|\nabla I v\|_{L^2(Q)}^2.$$

This shows that the energy of $I v$ on the triangle T is controlled by the energy of $I v$ on the neighboring channel Q and the assertion follows from the first part of the proof. \square

The stability of interpolation operator I implies the following approximation properties.

Lemma 3.4 (Approximation properties of the interpolation). *Let $u \in V$. Then the following estimates hold with constants independent of the (local) mesh size h and the diameter of the discs in \mathcal{B} . For all $Q \in \Omega$,*

$$\|h_Q^{-1}(u - Iu)\|_{L^2(Q)} \lesssim \|u\|_{H^1(Q)}. \quad (3.4)$$

For all $T \in \mathcal{T}$,

$$\|h_T^{-1}(u - Iu)\|_{L^2(T)} \lesssim \|u\|_{H^1(\omega_T)} \quad (3.5)$$

with the element patch

$$\omega_T := \cup \{Q \in \Omega : \bar{T} \cap \bar{Q} \neq \emptyset\}.$$

For all $E \in \mathcal{E}$,

$$\|u - Iu\|_{L^2(E)} \lesssim h_E^{1/2} \|u\|_{H^1(\omega_E)}. \quad (3.6)$$

We emphasize that the mesh size h_Q for $Q \in \mathcal{Q}$ is not a constant.

Proof. The localized Friedrichs inequality [20, Lemma A.1] shows that

$$\|u - Iu\|_{L^2(Q)} \lesssim \|\delta \nabla(u - Iu)\|_{L^2(Q)}$$

for any $Q \in \mathcal{Q}$ (cf. [20, Eq. (35)]). It is easily checked that the proof [20] may be modified so that assertion (3.4) holds on quadrilateral elements. The result (3.5) for triangles $T \in \mathcal{T}$ follows immediately from [20, Eq. (36)].

To prove (3.6), let $E \in \mathcal{E}$ and let $T \in \mathcal{T}$ be some triangle with edge E . According to [10], the trace inequality for H^1 functions yields

$$\|u - Iu\|_{L^2(E)} \lesssim h_E^{1/2} \|\nabla(u - Iu)\|_{L^2(T)} + h_E^{-1/2} \|u - Iu\|_{L^2(T)}. \quad (3.7)$$

The approximation properties of the nodal interpolation operator yield

$$h_T^{-1} \|u - Iu\|_{L^2(T)} \lesssim \|\nabla u\|_{L^2(\omega_T)}. \quad (3.8)$$

The combination of (3.7) and (3.8) is (3.6). \square

3.2 Proof of Reliability

We define the residual $\mathcal{R}es \in V^*$ for all $v \in V$ by

$$\mathcal{R}es(v) := a(e, v) = F(v) - a(u_{\text{NFEM}}, v). \quad (3.9)$$

Note that the test space of the Galerkin method V employed to obtain u_{NFEM} is in the kernel of the residual. Together with some interpolation estimates, the Galerkin orthogonality $S \subset \ker \mathcal{R}es$ is key in the derivation of residual estimators.

Since $Iv \in S$ is an admissible test function for any $v \in V$, Galerkin orthogonality and element-wise integration by parts yield

$$a(e, v) = a(e, v - Iv).$$

We write the integrals of (3.9) as sum over the elements of \mathcal{G} which gives, for $v \in V$,

$$a(e, v - Iv) = \sum_{G \in \mathcal{G}} \left\{ \int_G f(v - Iv) \, dx - \int_G \nabla u_{\text{NFEM}} \cdot \nabla(v - Iv) \, dx \right\}.$$

Recall that $(v - Iv)|_{\partial(\cup \mathcal{B}_{\text{inc}})} = 0$ from (3.2). Then, integration by parts and rearranging terms yield

$$a(e, v - Iv) = \sum_{G \in \mathcal{G}} \int_G r_G(v - Iv) \, dx + \sum_{E \in \mathcal{E}_{\text{int}}} \int_E r_E(v - Iv) \, ds.$$

By use of Cauchy–Schwarz,

$$a(e, v) \leq \sum_{G \in \mathcal{G}} \|h_G r_G\|_{L^2(G)} \|h_G^{-1}(v - Iv)\|_{L^2(G)} + \sum_{E \in \mathcal{E}_{\text{int}}} \|r_E\|_{L^2(E)} \|v - Iv\|_{L^2(E)}.$$

With the interpolation estimates of Lemma 3.4 and another application of Cauchy–Schwarz, we arrive at

$$a(e, v) \lesssim \|v\|_{H^1(\Omega)} \left\{ \sum_{G \in \mathcal{G}} \|h_G r_G\|_{L^2(G)}^2 + \sum_{E \in \mathcal{E}_{\text{int}}} h_E \|r_E\|_{L^2(E)}^2 \right\}^{1/2}.$$

With $v = e$ we obtain the error estimate

$$\|\nabla e\|_{L^2(\Omega)}^2 \lesssim \sum_{G \in \mathcal{G}} \|h_G r_G\|_{L^2(G)}^2 + \sum_{E \in \mathcal{E}_{\text{int}}} h_E \|r_E\|_{L^2(E)}^2 = \eta^2.$$

3.3 Proof of Efficiency

The efficiency of η can be derived by a combination of standard arguments, see [22], and the interpolation error estimates of Section 3.1.

We denote by $\psi_G \in H_0^1(G)$ the usual element bubble function on $G \in \mathcal{G}$ and by $\psi_E \in H_0^1(\omega_E)$ the usual edge bubble function with support on the patch ω_E of edge $E \in \mathcal{E}$, see [22] for details. The definition of bubble functions on triangular and quadrilateral elements can also be found in [1]. Note that an edge bubble function ψ_E is continuous along $E \in \mathcal{E}$ in both configurations which may occur, i.e., for some $T_1, T_2 \in \mathcal{T}$ and $Q \in \Omega$, $E = T_1 \cap T_2$ or $E = T_1 \cap Q$.

In any case, the usual estimates for edge bubbles hold, see, e.g., [22]. For $Q \in \Omega$, we set $\psi_Q = \psi_{Q_{\text{ref}}} \circ J_Q^{-1}$ the pull-back onto the bubble function of the reference rectangle. Local efficiency is first shown for the volume residual, then for the edge residual.

For some element $G \in \mathcal{G}$, we set $v_G := \psi_G \tilde{r}_G$ and deduce

$$\begin{aligned} \|h_G \tilde{r}_G\|_{L^2(G)}^2 &\leq \int_G h_G^2 \tilde{r}_G v_G \, dx = \mathcal{R}es(h_G^2 v_G) - \int_G (f - f_G) h_G^2 v_G \, dx \\ &\leq \|\nabla(u - u_{\text{NFEM}})\|_{L^2(G)} \|\nabla(h_G^2 v_G)\|_{L^2(G)} + \|h_G(f - f_G)\|_{L^2(G)} \|h_G v_G\|_{L^2(G)} \\ &\leq (\|\nabla e\|_{L^2(G)} + \|h_G(f - f_G)\|_{L^2(G)}) \|h_G \tilde{r}_G\|_{L^2(G)}. \end{aligned}$$

Here, we have used the inverse inequality $\|\nabla(h_G^2 \tilde{r}_G)\|_{L^2(G)} \leq \|h_G \tilde{r}_G\|_{L^2(G)}$ on $G \in \mathcal{G}$ for any $v \in V(G)$ with a constant independent of the mesh size h_G and $h_G \nabla \psi_G \leq C$ with C depending on anisotropy $\text{diam}(G)/\sqrt{|G|}$. Such inverse estimates are standard for classical FEM and can be proved with techniques as in [20]. With the split

$$\|h_G r_G\|_{L^2(G)} \leq \|h_G \tilde{r}_G\|_{L^2(G)} + \|h_G(f - f_G)\|_{L^2(G)}$$

we obtain

$$\|h_G r_G\|_{L^2(G)} \leq \|\nabla e\|_{L^2(G)} + \text{osc}(f, G). \quad (3.10)$$

Note that along some edge $E \in \mathcal{E} \setminus \Gamma_D$ with $E = G_+ \cap G_-$, $G_+, G_- \in \mathcal{G}$, the jump $[\nabla u_{\text{NFEM}} \cdot n_E]_E$ is not constant. Let $v_E : \omega_E \rightarrow \mathbb{R}$ be the piecewise (with regard to G_+ and G_-) harmonic function with $v_E|_E = \psi_E [\nabla u_{\text{NFEM}} \cdot n_E]_E$ and $v_E|_{\partial\omega_E} = 0$. We derive as before

$$\begin{aligned} \|[\nabla u_{\text{NFEM}} \cdot n_E]_E\|_{L^2(E)}^2 &\leq \int_E [\nabla u_{\text{NFEM}} \cdot n_E]_E v_E \, ds = \int_{\omega_E} r_G v_E \, dx - \mathcal{R}es(v_E) \\ &\leq \|r_G\|_{L^2(\omega_E)} \|v_E\|_{L^2(\omega_E)} + \|\nabla e\|_{L^2(\omega_E)} \|\nabla v_E\|_{L^2(\omega_E)} \\ &\leq (h_E^{1/2} \|r_G\|_{L^2(\omega_E)} + h_E^{-1/2} \|\nabla e\|_{L^2(\omega_E)}) \|[\nabla u_{\text{NFEM}} \cdot n_E]_E\|_{L^2(E)}. \end{aligned}$$

The constant in the trace inequality depends on anisotropy of the element. This, (3.10) and a triangle inequality yield the assertion

$$\|[\nabla u_{\text{NFEM}} \cdot n_E]_E\|_{L^2(E)} \leq h_E^{1/2} \|f + \text{div}_{\mathcal{G}} \nabla u_{\text{NFEM}}\|_{L^2(\omega_E)} + h_E^{-1/2} \|\nabla e\|_{L^2(\omega_E)}.$$

Note that edges on the Neumann boundary can be treated in the same way.

4 Numerical Examples

This section is concerned with the practical assessment of the Network FEM described in Section 2. In Section 4.1, the percolation effect is demonstrated with domains with many densely packed inclusions. When the density of filler particles becomes high enough, connected paths through the domain can emanate which leads to a strong increase of the energy of the solution. We demonstrate that the energy of the solution u_{NFEM} depends on the density of particles and on their distance. It is illustrated numerically that the error is basically independent of the inclusion distance and thus of the energy $\mathcal{E}(u_{\text{NFEM}})$.

In Section 4.2 we compare the simulation of inclusions distributed in a structured and in a random way. The striking observation is that for identical volume fraction, i.e., the same number of inclusions, the two settings exhibit completely different properties. While percolation can be seen in the structured case, the energy $\mathcal{E}(u_{\text{NFEM}})$ stays nearly constant with random particle distributions. Since many methods for multiscale problems like several popular multiscale FEM and classical homogenization assume periodicity of the microscale in the limit, this finding strongly supports the explicit resolution of the actual microscale structure as pursued in the presented Network FEM.

For all computations, model problem (1.1) on the square domain $\Omega^* := [0, 1]^2$ with equi-sized inclusions is employed. On the left and right boundary, homogeneous Neumann boundary data are prescribed. Dirichlet data is set on the top and bottom boundaries with $u|_{y=0} = 0$ and $u|_{y=1} = 1$. Since the problem can be regarded as stochastic due to the randomly distributed particles, a set of realizations is computed and statistics are evaluated afterwards.

In order to obtain an adequate boundary representation with the grid, we mirror the perforated domain Ω along all four sides and also along the four corners of Ω^* . We then apply the algorithm described in Section 2.1. Next, quadrilaterals in \mathcal{Q} which intersect $\partial\Omega^*$ are identified and their projections onto Ω^* are collected in the set of boundary quadrilaterals $\mathcal{Q}_{\partial\Omega}$. Likewise, triangles in \mathcal{T} whose projection onto Ω^* does not deteriorate are collected in $\mathcal{T}_{\partial\Omega}$. All other new quadrilaterals and all vertices outside of Ω^* which are not connected to quadrilaterals in $\mathcal{Q}_{\partial\Omega}$ are discarded.

Note that there are different approaches for the treatment of the boundaries. One possibility is the insertion of nodes (discs with vanishing radius) onto the boundaries. Another approach is the notion of quasi-discs as described, e.g., in [5]. A quasi-disc results from an inclusion (close to the boundary) whose projection rays onto the boundary do not intersect any other inclusion. The projection on the boundary then is handled like an inclusion inside the domain.

Remark 4.1. Care has to be exercised to achieve a sufficiently high accuracy for the quadrature on the quadrilateral elements of \mathcal{Q} since the transformation map can be highly non-linear due to inclusions with very small distance. This is particularly critical for the evaluation of integrals of second derivatives as required for the residual error estimator. We employ an adaptive quadrature scheme which subdivides each $T \in \mathcal{Q}$ into $O(\log \delta^{-1})$ isotropic elements for which a conventional quadrature rule results in high accuracy. Here, δ is the distance of the two inclusions which are connected by T . Thus, the adapted quadrature does not adversely affect the quasi-optimal complexity of the method.

4.1 Percolation

In this experiment, we assume a set of equally sized inclusions with increasing density. More specifically, the volume fraction $|\mathcal{B}_{\text{inc}}|/|\Omega^*|$ is increased successively up to a value where connected paths of (nearly) touching inclusions are formed. Along these, unhindered decrease of energy is possible and a sudden change of effective conductivity is to be expected. The percolation phenomenon becomes apparent from the energy graphs in Figure 5. In order to facilitate a dense packing, the distribution of inclusions is generated by starting with a structured distribution on a regular lattice and successive removal of random inclusions until the desired density is reached. Depicted in Figure 5 are the energy and error graphs for inclusions with distances $\varepsilon = 10^{-2}, 10^{-4}, 10^{-6}, 10^{-8}$. Additionally, upper and lower energy bounds together with the averaged a posteriori error estimator are plotted. We average with regard to 100 realizations of the random domain with fixed volume fraction. It is expected that the maximal energy increases with smaller distances of inclusions. This is verified numerically in the graphs. The moderate decrease of the a posteriori error estimator can be attributed to the increased approximation quality with more inclusions since these are equivalent to degrees of freedom.

This standard setting can frequently be found in the literature; it is, for instance, examined in [5, 18, 19].

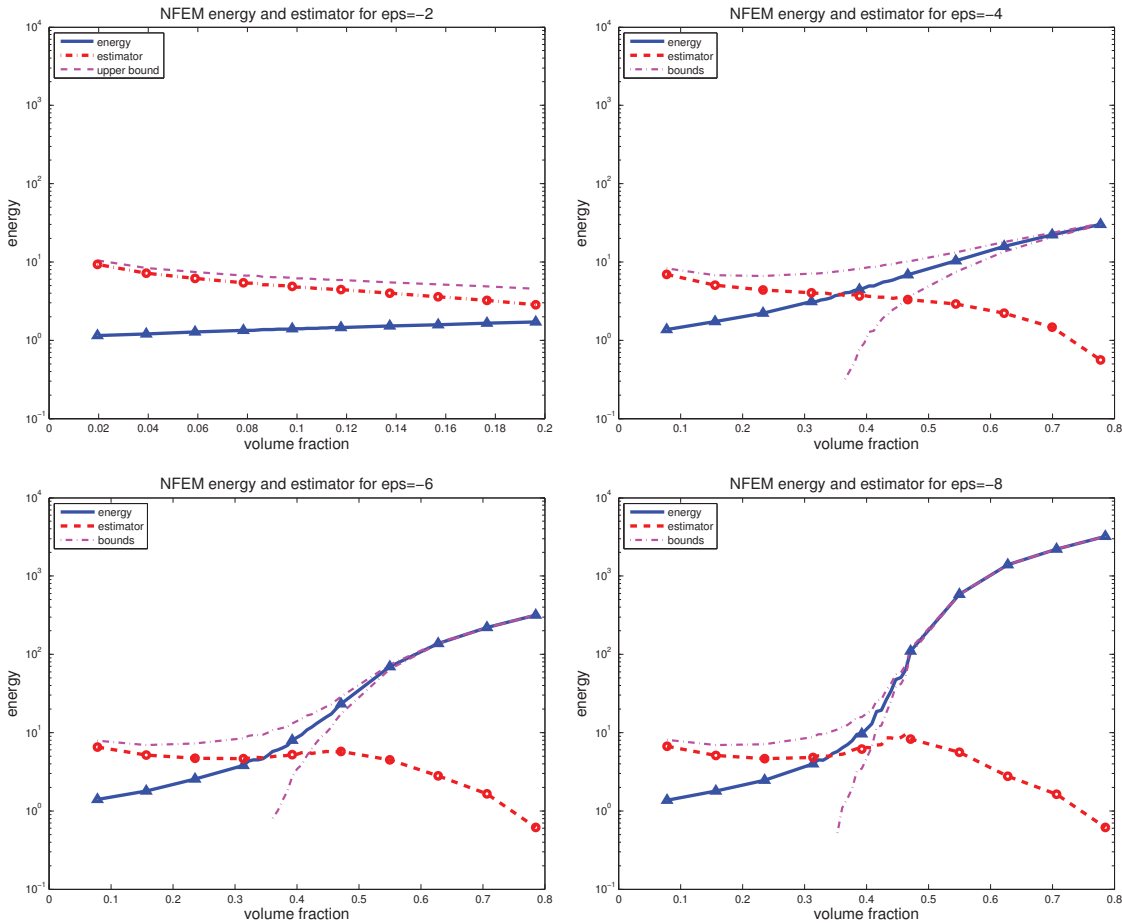


Figure 5. Average energy and a posteriori error estimator for a structured distribution of inclusions with distances $\epsilon = 10^{-2}, 10^{-4}, 10^{-6}, 10^{-8}$. Upper and lower bounds for the averaged energy due to the error estimator.

4.2 Model Validation

This subsection is concerned with the comparison of some structured and some random distribution of inclusions with equal volume fraction up to $\text{VF} = 0.5$ for all domains. Our experiments illustrate that a distribution based on a structured setting of Figure 6 (left) exhibits fundamentally different behavior than a random distribution as displayed in Figure 6 (right). In particular, the percolation effect which is based on a very dense packing and the formation of some closed path through the domain as discussed in the last section cannot be observed with entirely randomly dispersed inclusions although the same amount of inclusions exists in the domain. In Figure 7, the energy graphs for the structured and the random case are depicted. We also plot the upper bound of the energy subject to the a posteriori error estimator, respectively.

This interesting finding questions the assumption of a structured distribution or periodicity in the limit which is the basis for homogenization and many multiscale approaches.

5 Conclusions and Outlook

This last section is devoted to some conclusions regarding the presented Network FEM. The method benefits from its relation to network methods as well as from its features inherited from classical FEM. Of the former, the resolution of the small geometrical features of the domain with quasi-optimal complexity is derived. The latter enables the reliable and efficient error control for the discretization error with some computable a pos-

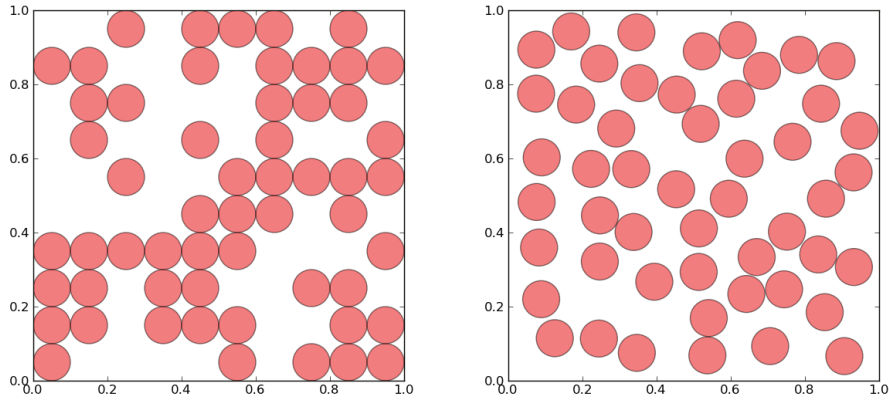


Figure 6. Structured and random test domains with equal volume fraction.

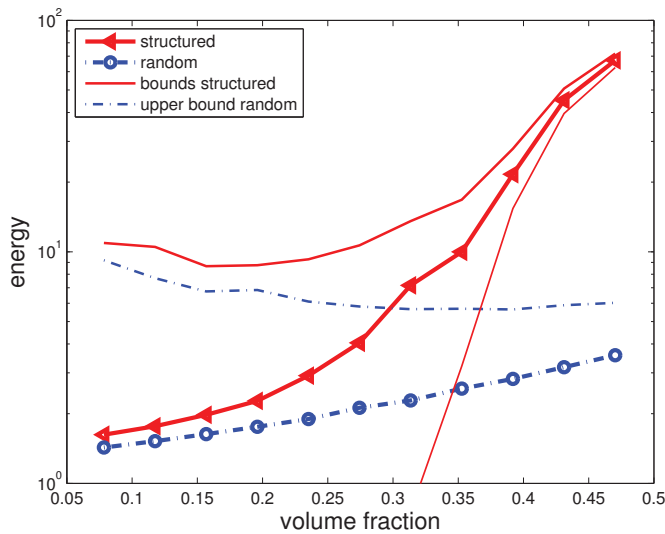


Figure 7. Energy for structured and random test domains with energy upper bound due to a posteriori error estimator.

teriori error estimator. The Network FEM on the one hand is very flexible with regard to the size and shape of the inclusions and may be generalized easily to other settings. On the other hand, it does not suffer from the computational complexity induced by a possibly very fine mesh. It thus succeeds to combine favorable properties of the two related numerical methods.

The proposed method may be understood as a discretization model for the material behavior of composite materials. The computational complexity is minimal since it is proportional to the complexity of the data, i.e., the number of inclusions. At the same time, it sustains the critical structural material properties.

If, in addition to this structurally correct approximation, high accuracy or high resolution of the singular behavior is required, it is possible to devise adaptive algorithms with the aim to improve the approximation locally where the current error is large. An immediate approach would be to introduce additional vertices with radius zero wherever the error indicator exceeds a certain threshold. Since this only concerns triangular elements, a complicated remeshing of the entire domain could be avoided by a selective subdivision of marked elements. A detailed examination of possible refinement strategies and the resulting convergence properties of adaptive NFEM is left for future research.

Funding: This work was supported by the DFG Research Center Matheon Berlin through project C33.

References

- [1] M. Ainsworth and J. Oden, *A Posteriori Error Estimation in Finite Element Analysis*, John Wiley & Sons, New York, 2000.
- [2] F. Aurenhammer and R. Klein, Voronoi diagrams, in: *Handbook of Computational Geometry*, North-Holland, Amsterdam (2000), 201–290.
- [3] N. Bakhvalov and G. Panasenko, *Homogenization: Averaging Processes in Periodic Media*, Kluwer Academic Publishers, Dordrecht, 1989.
- [4] A. Bensoussan, J.-L. Lions and G. Papanicolaou, *Asymptotic Analysis for Periodic Structures*, North-Holland, Amsterdam, 1978.
- [5] L. Berlyand and A. Kolpakov, Network approximation in the limit of small interparticle distance of the effective properties of a high-contrast random dispersed composite, *Arch. Ration. Mech. Anal.* **159** (2001), no. 3, 179–227.
- [6] L. Berlyand, A. G. Kolpakov and A. Novikov, *Introduction to the Network Approximation Method for Materials Modeling*, Encyclopedia Math. Appl. 148, Cambridge University Press, Cambridge, 2013.
- [7] L. Berlyand and A. Novikov, Error of the network approximation for densely packed composites with irregular geometry, *SIAM J. Math. Anal.* **34** (2002), no. 2, 385–408.
- [8] L. Borcea and G. C. Papanicolaou, Network approximation for transport properties of high contrast materials, *SIAM J. Appl. Math.* **58** (1998), no. 2, 501–539.
- [9] C. Carstensen, M. Eigel, R. H. W. Hoppe and C. Löbhard, A review of unified a posteriori finite element error control, *Numer. Math. Theory Methods Appl.* **5** (2012), no. 4, 509–558.
- [10] C. Carstensen and S. A. Funken, Constants in Clément-interpolation error and residual based a posteriori error estimates in finite element methods, *East-West J. Numer. Math.* **8** (2000), no. 3, 153–175.
- [11] D. Cioranescu and P. Donato, *An Introduction to Homogenization*, Oxford University Press, Oxford, 2000.
- [12] H. Edelsbrunner, *Geometry and Topology for Mesh Generation*, Cambridge Monogr. Appl. Comput. Math. 7, Cambridge University Press, Cambridge, 2006. Reprint of the 2001 original.
- [13] I. Ekeland and R. Temam, *Convex Analysis and Variational Problems*, Stud. Math. Appl. 1, North-Holland, Amsterdam, 1976.
- [14] G. Grimmett, *Percolation*, 2nd ed., Grundlehren Math. Wiss. 321, Springer, Berlin, 1999.
- [15] H. Keller and D. Sachs, Calculations of the conductivity of a medium containing cylindrical inclusions, *J. Appl. Phys.* **35** (1964), 537–538.
- [16] J. Keller, Conductivity of a medium containing a dense array of perfectly conducting spheres or cylinders or nonconducting cylinders, *J. Appl. Phys.* **34** (1963), no. 4, 991–993.
- [17] H. Kesten, *Percolation Theory for Mathematicians*, Birkhäuser, Basel, 1992.
- [18] A. Kolpakov, Numerical verification of the existence of the energy-concentration effect in a high-contrast heavy-charged composite material, *J. Eng. Phys. Thermophys.* **80** (2007), 812–819.
- [19] A. A. Kolpakov and A. G. Kolpakov, *Capacity and Transport in Contrast Composite Structures*, CRC Press, Boca Raton, 2010.
- [20] D. Peterseim, Robustness of finite element simulations in densely packed random particle composites, *Networks Heterogeneous Media* **7** (2012), no. 1, 113–126.
- [21] D. Peterseim and C. Carstensen, Finite element network approximation of conductivity in particle composites, *Numer. Math.* **124** (2013), no. 1, 73–97.
- [22] R. Verfürth, *A Review of A Posteriori Error Estimation and Adaptive Mesh-Refinement Techniques*, Wiley-Teubner, Chichester, 1996.
- [23] V. V. Zhikov, S. M. Kozlov and O. A. Olejnik, *Homogenization of Differential Operators and Integral Functionals*, Springer, Berlin, 1994.

Received September 30, 2014; accepted October 2, 2014.